Available online at www.sciencedirect.com

Manufacturing Letters

Manufacturing Letters 41 (2024) 730–741

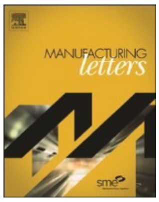

52nd SME North American Manufacturing Research Conference (NAMRC 52, 2024)

Thermal profile modeling and microstructural evolution in laser processing of Inconel 625 plates by comparison of analytical and numerical methods

Stephanie B. Lawson[a,b], Milad Ghayoor[a,b], Xianzhe Fu[a,b], Ali Tabei[a,b], Andy Fan[a,b], Somayeh Pasebani[a,b,*]

[a]School of Mechanical, Industrial, and Manufacturing Engineering, Oregon State University, Corvallis OR, USA [b]Advanced Technology and Manufacturing Institute (ATAMI), Corvallis OR, USA

Abstract

Microstructural evolution of materials under specified process conditions and parameters can be predicted by thermal modeling of additive manufacturing laser processes. The objective of this study was to develop, analyze and compare two methods for prediction: an analytical method and a numerical method for laser processing of Inconel 625 material. These methods were compared with experimental results for thermal profiling, and the effect of thermal profiles on microstructure of the experimental samples was explored. Maximum temperature and cooling rate of the numerical method were shown in good agreement, while the analytical method proved more challenging when compared to the experimental results for three laser parameters. Cooling curves were correlated with microstructure in terms of grain size, morphology, and orientation, with findings trending with parameter adjustments. This research supports the numerical modeling approach as a method for examining optimal laser processing conditions for Inconel 625 that is ideally suited for complex fluid flow analyses.

Keywords: Additive Manufacturing; Analytical Modeling; Inconel 625; Microstructure Evolution; Numerical Modeling; Thermal Profile

1. Introduction

Thermal history (e.g., cooling rates, temperature gradient) associated with laser processing dictates microstructural evolution patterns [1, 2] such as segregation [3, 4] or crystallographic texture [5]. Comprehensive review of this relationship in additively manufactured materials is provided by Clare et al. [6]. However, temperature and microstructural evolution are difficult to experimentally measure in real-time during the laser metal additive manufacturing (AM) process due to intrinsic rapid heating and cooling rates [7, 8]. This challenge has led to the emerging opportunity for methods outside of physical experimentation, such as computational modeling, to be utilized as a viable way to explore the process-structure-property relationships in AM processes [9].

There are two main approaches to computational modeling: analytical and numerical. While analytical modeling provides a quick and reliable way of gathering thermal information for

* Corresponding author. Tel.: +1-541-737-3685 ; fax: +1-541-737-2600.
E-mail address: somayeh.pasebani@oregonstate.edu (Somayeh Pasebani).

welding applications, this approach is not ideal in situations where analysis of microstructure or profiling is required due to highly simplified assumptions for what are often highly complex laser AM processes. On the other hand, numerical modeling, though costly from a computational aspect, is based on constitutive equations developed and solved numerically, and provides more realistic physical results because of the inclusion of fluid flow analysis. Promoppatum et al. [10] provides comparison of analytical and numerical approaches to predict microstructure and while both were found to perform well for ther-
mal and microstructural prediction at low energy inputs (less than 200-300 W), it was found that high energy input processing renders the analytical approach less accurate than the numerical approach.

Early research on modeling heat source for welding applications was done through the work of researchers such as Rosenthal [11] and Goldak [12]. As a popular method for modeling, Goldak's double-elliptical model has been a foundational model for researchers to build upon [13, 14, 15]. Gery et al. [16] incorporates C++ programming into Goldak's method to develop 2D and 3D finite element modeling that defines a moving distributed heat source for plate butt welding processes. Predicted peak temperatures were higher for the 2D model than those predicted in the 3D model, but no experiments were completed in the study. Bag et al. [17] incorporates Goldak's method into a conduction mode heat transfer numerical model with adaptive volumetric heat sourcing for analyses of weld pool dimensions. By using the conduction mode of heat transfer in attempt to eliminate the need of a-priori knowledge of heat source parameters, the numerical model was shown to provide information on effects of process parameters on weld pool dimensions. Challenges were shown to exist in predicting weld pool shapes, thus providing a model useful for fast a-priori understandings for influences of process parameters on laser spot welding processes. Mirkoohi et al. [18] provides five specific heat source models constructed through the Goldak method which are compared for accuracy, and findings concluded that the double-elliptical model had the best performance to predict the melt pool geometry and temperature gradients for a wide range of laser parameters. Although the modeling developed by Mirkoohi et al. [18] is able to provide temperature specific information, it lacks a dynamic component to capture thermal profiling of laser processes. Nevertheless, all of these methods for modeling continue to be customized and updated for specific applications and material combinations, emphasizing the usefulness of modeling for AM applications.

In an attempt to predict microstructure based on thermal impact, time-dependent material phase transformation becomes critical in assessing final performance for materials such as nickel-based alloys, where in welding processes alloy elements can segregate and result in varying heating and cooling rates throughout the weld bead. Thermal history and microstructural evolution (grain morphology, grain size, and texture) considering time dependency of material phase transformation has rarely been studied [19]. Youseff et al. [20] developed a threedimensional finite-difference analysis model to predict thermal and clad layer morphology and geometry evolution of laser powder cladding of Ti6Al4V alloy. This model led to the conclusion that increasing the parameters of laser power and scan speed increases the heating and cooling rates. Laser power contributed most to the peak melt-pool and heat affected zone temperatures when compared to experimental results, and the quick movement of the scanning laser beam lead to the scan speed having more effect on cooling rate than power.

Due to inevitable variation within the processing environment, work by Huang et al. investigated process parameters for influence on localized transient thermal characteristics (temperature, cooling rate) and solidification parameters (thermal gradient (G) and solidification rate (R)) in order to rapidly predict microstructural evolution for SS316L and Inconel 625 (INC625) [1]. Thermal characteristics and solidification parameters were simulated, and evidence of correlating higher cooling rate (G×R) to finer microstructure were reported. Though this analytical model proved a viable option for in-situ prediction of thermal characteristics and realtime microstructural control, further work on optimizing calculation time was suggested. The role of melt pool geometry, peak temperatures, temperature gradients and cooling rates in laser processing of INC625 on microstructure were predicted through comparing a 3D finite volume modeling method (based on the heat conduction solidification equation model) with and without fluid dynamics with experimental validation [21].

The main drawback of simulating AM processes is the computational cost for accurate predictions of process and microstructure. However, optimizing the development and runtime of a simulation has been shown to be effective at overcoming this drawback. Simulation optimization has been studied by investigating mesh strategies and computational cost for laser processing, providing potential direction for increasing efficiency for process parameter optimization [22]. Optimization of parameters for input into Goldak's (1984) analytical doubleellipsoidal heat source model was performed based on isoparametric transformation and computer graphics [23]. The effects of fluid flow on weld pool shapes were not considered, thus eliminating information for microstructure prediction through fluid flow analysis.

Despite these studies showing extensive evidence that modeling is an effective means to explore process parameter and thermal influence in AM laser processes, a gap remains in finding a mode for advancing AM modeling to explore the process-structure-property relationship in an optimized and cost-effective way. For time-dependent material phase transformation in popular materials such as nickel-based alloys, the importance in choosing the correct computational approach is lacking in literature. Studies show the viability of computational models as a valuable option to capture AM processes while reducing experimental costs. However as a first step, few studies compare the analytical and numerical approach against each other, with the aim to explore processstructure-property relationships through comparison of modeling results with experimental validations.

In the present study, two approaches for predicting thermal history in materials due to laser processing are presented and compared. As a popular material choice for application in extreme environments such as aerospace, marine engineering, and nuclear reactors where high strength and corrosion resistance properties are needed, INC625 was chosen as a study material due to the popularity in additive manufacturing where high heating and cooling rates of laser processing can drastically impact microstructure and ultimately final performance. First, modeling of laser plate scanning using INC625 by analytical and numerical method are proposed and compared. Next, both methods are compared and validated with experimental results considering thermal history and cooling trends. Finally, microstructural evolution of INC625 on experimental results is discussed as it relates to the cooling curve trends found in each case examined as further means of validating the accuracy and utility of each method towards material property analysis.

2. Modeling Methodology

2.1. Analytical Method

The analytical method that is presented is based on the closed-form solution (temperature as a function of input parameters) previously reported by Goldak [12] and is coded for different heat source geometries (shown in Figure 1 and described in Equation 1),

$q(x,y,z,t) =$

$6PV_{\eta}\sqrt{3}$ $c f_{rf} f$ $exp\,exp$ $--33((xx--cVtVtr2f))2--$

$33 ayay22 -- 33 bzbz22$ $forx forx <> vtvt$ (1) $\pi\, \pi ab \times c\, C$

222 222

where subindex i represents either f (front) or r (rear), and f_f and f_r are the relative amount of heat applied to the front and rear portion of the heat source. The constraint shown in Equation 2 is commonly applied [15] to ensure continuity of heat deposition, q, across the heat source.

$$\frac{f_f}{c_f} = \frac{f_r}{c_r} \quad (2)$$

Building on Mirkoohi et al.'s [18] double-elliptical heat source model, the current work expands the thermal analysis into dynamic time-dependent multi-track laser scans on an INC625 plate. Mirkoohi et al.'s (2019) modeling approach is static. The presented method incorporates the movement of the fiber laser, providing a thermal history at any point in the specified area of interest, rather than temperature profile at a single point in time. The chosen approach utilizes the analytical method to generate a double-elliptical heat source model, which is a geometric heat source model of a 3D doubleellipsoidal shape with a discretized mesh used to solve for temperature. In this work, heat loss due to convection and radiation was not considered, and heat conduction is considered through the semi-infinite body. Solving for the temperature field from the double elliptical heat source is done using a Green's function approach shown in Equation 3.

$$T(x,y,z,t) = T_o + \frac{3P\eta\sqrt{3}}{\pi\sqrt{\pi}\rho C} \times \int_0^t \frac{exp\left(-3\frac{y^2}{12D(t')+a^2} - 3\frac{z^2}{12D(t-t')+b^2}\right)}{\sqrt{12D(t-t')+a^2}\sqrt{12D(t-t')+b^2}} \times \left[f_r A_r(1-B_r) + f_f A_f(1+B_r)\right] dt' \quad (3)$$

where modified heat capacity is considered in the thermal diffusivity term, D, and,

$$A(i) = A(x,t,t',c_i) = \frac{q\, exp\left(-3\frac{(x-Vt)^2}{12D(t-t')+c_i^2}\right)}{2\sqrt{12D(t-t')+c_i^2}} \quad (4)$$

$c_i(x-Vt)$

$$B(i) = B(x,t,t',c_i) = erf\ \frac{q}{2\sqrt{12D(t-t') + c_i^2 * D(t-t')}}$$

This model can be used to predict the temperature at each location (x,y,z) at each timestep t that results from the heat source applied at the timestep t' and location (x',y',z'). When applied at distinct timesteps, temperature in and around the heat affected zone (HAZ) was predicted.

For the developed model, this heat source model is applied to the entire plate to include temperatures of both the HAZ and the surrounding areas to this zone. At each timestep, the temperature at each node is updated according to the model calculations with temperature-dependent properties of modified heat capacity and thermal conductivity. Modified heat capacity allows energy deposited into the baseplate by the laser generated on the surface of the plate. This mesh also allowed for temperature data at the nodes within this temperature field to be interpreted for analysis and comparison with the numerical model and experimental results.

to be taken into account by considering the latent heat of fusion during phase transformation in the heat capacity properties. The modified heat capacity is expressed in Equation 5:

$$C_p^m = C_p(T) + L_f \frac{\delta f}{\delta T} \quad (5)$$

distinct equations that solve exactly for specific points. Unlike the numerical model, the mesh did not need to resolve a heat source model. Rather, the mesh had to have a resolution high enough to capture an accurate temperature field for the melt pool and the HAZ. Shown in Figure 2, a mesh of 0.152 mm was chosen, providing for a unique temperature field to be

2.2. Numerical Method

Developed using the commercial computational fluid dynamics (CFD) software Flow-3D, the numerical method uses

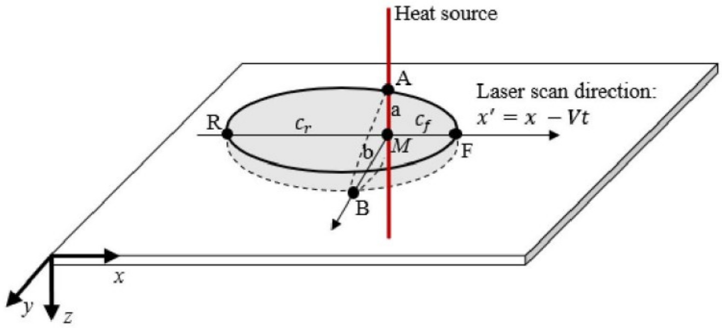

Figure 1. Closed-form solution heat source model [12].

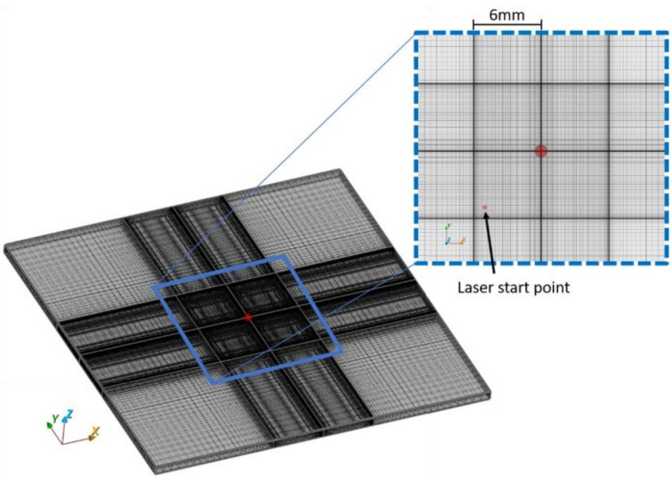

Figure 2. Inconel 625 plate scan meshing with closeup of laser point.

where C_p is heat capacity, L_f is latent heat of fusion, f is the liquid fraction taking into account the liquidus and solidus temperatures of the material [12].

The analytical method for predicting temperatures of laser AM processes through heat source modeling provides for

the Fractional-Area-Volume-Obstacle-Representation (FAVOR™) method and the Volume-of-Fluid (VOF) method as a volumebased approach to computational modeling. The VOF method provides (1) the surface position, (2) an algorithm to track the surface as it moves along the mesh, and (3) a mode for applying boundary conditions at the surface. The FAVOR™ method utilizes a simple rectangular grid construction mesh design. Reasonable temperature readings were assumed through the limitation of maximum vapor pressure in the numerical model. Temperaturedependent material properties were considered for both the molten and solid materials. These properties are thermal diffusivity, and surface tension.

In CFD the governing equations are nonlinear, and the number of unknown variables is typically large in comparison to other modeling methods. Under these conditions, implicitly formulated equations are solved using iterative techniques for time-dependent process solutions. Implicit solution methods

were chosen for calculating the heat transfer and surface where (G_x,G_y,G_z) are accelerations of the body, (f_x, f_y, f_z) are tension for two reasons: 1) stability is maintained with no limit viscous accelerations, (u_w,v_w,w_w) are the velocity components to the size of the time step, allowing for large time step sizes where motions of each time step are calculated using the where available; 2) accuracy increases due to sufficiently small force and velocity data from the previous time step. The

changes in time steps from one iteration to the next in order to velocity of the fluid at the surface of the source relative to

the maintain convergence [24, 25]. source itself is $U_s = (u_s,v_s,w_s)$.

Differential equations that are solved in the numerical In order to evaluate heat transfer, the same general model are written in terms of Cartesian coordinates (x,y,z). The principle for predicting heat transfer and therefore

general mass continuity equation is:

temperature in the numerical method as in the analytical model. The heat conduction equation is the basis of temperature prediction. In the numerical approach utilizing a first-order implicit method, the heat conduction equation can be discretized as:

$$\partial\rho + \frac{\partial}{\partial t} \quad \partial \quad \partial \quad + \frac{\partial}{} (\rho w A\ ) + \xi \frac{\rho\mu A_x}{} \quad V_f \quad (\rho\mu A_x)+R\ \rho \quad vA_{yz} \quad x \quad \partial y \quad \partial z \quad x \quad = D_T + D_S \tag{6}$$

$$D \frac{T_{in++11,j,k} - 2T_{in,+j,k1} + 2T_{in-+11,j,k}}{\Delta x2} + \frac{T_{in,+j+11,k} - 2T_{in,+j,k1} + 2T_{in,+j-11,k}}{\Delta y2} + \frac{T_{in,+j,k1+1}2T_{in,+j,k1} + 2T_{in,+j,k1-1}\ !}{\Delta z2} \quad D \quad + \_Q(x,y,z,t) = \frac{T_{in,+j,k1} - T_{in,j,k}}{} \tag{8}$$

where, (A_x, A_y, A_z) are the fractional areas open to flow in the corresponding (x,y,z) directions, with the velocity components (u,v,w) in Cartesian coordinates. V_f is the fractional volume open to flow, ρ is the density (evaluated as a function of temperature), D_T is the turbulent diffusion term, and D_S is the mass source.

Motion is accounted for by utilizing the Navier-Stokes vector $k\ \Delta t$ equations of motion. The equations are adapted for the fluid velocity components (u,v,w) in (x,y,z) directions as:

Mesh sizing was designed to analyze how the solution of the

$$\partial u \quad 1^{(} \quad \partial u$$

flow field in the form of pressure at the free surface changes.

$$1\ \partial p \quad D$$ set with a zero-gradient condition at the boundary as well as a

$$= - + G_z + f_z - (w - w_w - \delta w_s)\ \rho\ \partial z\ \rho V_F$$ zerovelocity condition normal to the boundary. The upper z boundary was set to follow a hydrostatic distribution with

) [2] Balance determined based on the ∂u ∂u $A_y v$ ∂t + V_F uA^x ∂x + experiment xV and mesh sizing

$$+ wA_z \qquad \frac{D_S}{\rho V_F}(u - u_w - \delta u_s) \quad \frac{\partial v}{\partial y} + wA_z \frac{\partial u}{\partial z} - \xi \frac{A_y uv}{xV_F} \quad \frac{D_S}{\rho V_F}(v - v_w - \delta v_s) \quad \frac{\partial w}{\partial y} + wA_z \frac{\partial w}{\partial z} \tag{7}$$

$-\frac{1}{\rho}\frac{\partial p}{\partial x}$ = – + G^x + f^x – ρ ∂x y

$\frac{1}{y}$ ∂p = – (R) + s y ∂v

between the resolution and computation time of the model was specific details of the including output needs for maximum temperature $vA^yR\partial y$ ∂z − ξ appropriate to capture laser spot size.

Maximum time steps were set to 0.001 s and controlled by stability and convergence. Based on the outcome of these studies, a 10 mm x 10 mm square centered on the plate was set to a mesh size of 0.07 mm while the outside of the center 1

(∂v square cell size was increased to 0.1 mm. This allowed the ∂t + $V_F vA_x$ ∂x + vA_yR mesh of the plate to be designed to have high refinement within the area of the plate impacted by the 40 µm spot size laser, while areas uninfluenced by the laser were set to a larger cell size for reduced computation time.

$G_y + f - \rho$ ∂

Boundary conditions applied for all x and y faces included no-slip ∂w 1 (∂w condition at the boundary and a zero-velocity condition + vA R normal to the boundary. The heat transfer coefficient for these + – wA^x ∂t V_F ∂x wall boundaries was set to 18 W/(m^2 K), depicting a rigid substrate with convective heat loss. The lower z boundary was

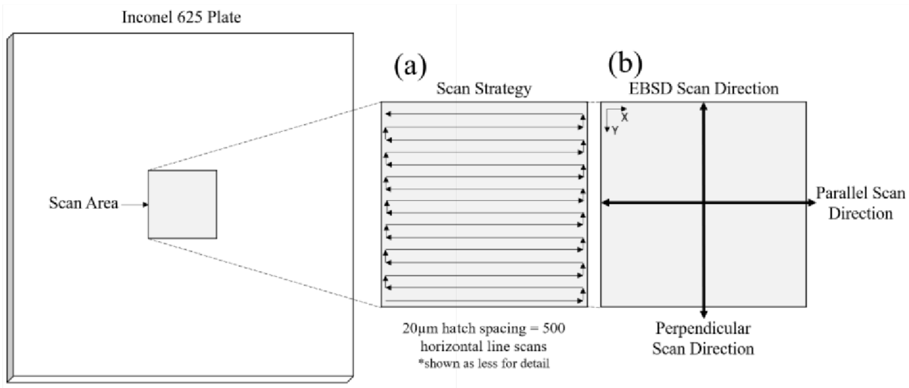

Figure 3. INC625 plate laser processing setup of (a) scan strategy and (b) demarcated EBSD scan direction.

pressure at the boundary set to standard atmospheric pressure of 1.013 e^5 Pa. Stagnation conditions outside the boundary were assumed in order to maintain zero velocity upstream from the boundary. Nitrogen shield gas was applied in the negative zdirection to match that of the equipment used in the experiment.

3. Experimental Methods

In order to investigate the effects of different laser powers on the thermal history and microstructural evolution, a 10 × 10 mm^2 geometry was laser cladded on the surface of an INC625 plate with the dimensions of 76 × 76 × 3 mm^3. Three cases were explored to examine the effects of laser powers 75 W, 150 W, and 225 W all with identical scan speeds of 200 mm/s and a scan strategy of zig-zag pattern with 20 µm hatch spacing. An example of the scan strategy is shown in Figure 3, where the INC625 plate was scanned starting in the lower XY plane of the scan area and moving horizontally along the X axis. This design was chosen to induce complex boundary conditions around the target position [26]. This scan strategy was chosen to guide laser parameters and movement. The process chosen for this research included parameters resulting in a 10 mm x 10 mm zigzag scanning pattern in order to provide enough heat to reach melting temperatures of INC625 within the power limitations of the experimental equipment.

The printer used for the experiment was an ORLAS CREATOR. The ORLAS suite software was adopted to assign different laser parameters to the 10 × 10 mm^2 geometry. A fiber laser with a maximum wattage of 250 W at 1070 nm and a spot size of 40 µm was used. An Optris PI 1M IR camera with a resolution of 56 × 72 ppi and 16 × 20 mm provided the measurement area that was used for temperature measurement by incorporating one pixel of data sized at 300 × 300 μm^2.

INC625 plates were used, and unless otherwise cited, all material properties were gathered from FLOW-3D® material database and are shown in Table 1. Surface tension is expressed through a gradient due to the high uncertainty of the parameter for INC625 in literature. This allowed for three levels of the surface tension to be simulated, representing no fluid flow, an intermediate value previously recommended in literature, and a higher predicted value [27].

Table 1. Thermal properties of INC625.

Material Property	INC625
Density (kg/m^3)*	8650.3 - 0.8098T [27]
Viscosity (kg/m s)	0.0072
Specific heat capacity (solid) (J/(kg K)*	428.38 + 0.23638T [27]
Specific heat capacity (liquid) (J/(kg K)*	750.65 [27]
Thermal conductivity (solid) (J/m s K)*	12.296 + 0.01472T [27]
Thermal conductivity (liquid) (J/m s K)*	8.9164 + 0.014743T [27]
Liquidus temperature (K)	1623.15
Solidus temperature (K)	1563.15
Latent heat (kJ/kg)	272
Surface tension gradient (kg/s^2)*	1.882, 1.877, 1.866, 1.855 [27]
Fluid absorption rate	0.3

*Function of temperature

3.1. Data Collection

The temperature at specific points of the plate was measured using IR camera, which was calibrated to commercially pure copper. Although the material used in this experiment was INC625, calibrating to pure copper is a common and widely accepted procedure for IR camera data collection [28]. The IR camera was calibrated to the melting temperature of copper melt temperature at phase change, matching the temperature measured at the melt phase to temperature of copper.

The points collected from the IR camera provided measurements of the melt pool and HAZ. Once the temperature data from the IR camera was collected, the data was processed and plotted on a temperature versus time graph to compare to the simulated data. The verification of both the analytical and numerical models was done through experimental validation using identical material and process parameters.

In order to determine thermal history data for comparing the models and experiments, an alignment of data obtained from models with collected IR camera data was expected. The use of IR camera to capture thermal history is a common practice with AM monitoring [27, 28], and has been utilized successfully at capturing the HAZ thermal measurements [29]. In the analytical code these values are predicted through the use of the double-elliptical model of a steady-state moving heat source, collected at the specific nodes corresponding to the area measured by the IR camera. Data was collected at the center of the plate, with a total square area of 300 x 300 m^2. For the numerical and analytical models, the average was taken from the temperature data obtained for each node within this area matching the IR camera collection.

The frame rate of the IR camera was 1000 Hz, and time steps for the measured data were at a rate of 1 data point every 0.001 s. A timestep of 0.001 s was chosen for the analytical code, providing a robust data set while maintaining efficiency of computation time. The numerical model was set for a maximum timestep of 0.001 s also, with the option of selecting data every 0.01 s for the output data. This was done to further mimic experimental setup while allowing the option to see greater details than experimental capabilities.

3.2. Microstructure Characterization

Each 10 × 10 mm^2 laser cladded geometry was cut from the experiment plate using wire electrical discharge machining (EDM) once perpendicular to the scan direction and once parallel to the scan direction to explore the depth of laser penetration. Each sample was mechanically polished using a standard metallography procedure to prepare cross-section samples of laser processed material for microstructural analysis. Electron backscatter diffraction (EBSD) was used to examine microstructure morphology through the evolution of increasing laser power for directions parallel and perpendicular to the laser scan (Fig. 3). The EBSD data collection was conducted using an Orientation Imaging Microscopy (OIM) Data Collection 7.2 software in FEI Quanta 3D operating at 15 kV accelerating voltage, 1.7 nA beam current, and a step size of 500 nm. The collected data were processed using OIM Analyses 7.2 software.

4. Results and Discussion

4.1. Data Output Validations

IR camera data collection provided imaging of the temperature field (Fig. 4-a), and an area of one pixel (300 x 300 μm^2) that was representative of the laser spot size was set as a basis for data collection among all three case studies. The analytical method was able to provide a distinct temperature field, shown in Figure 4-b, where data was gathered to represent the valid nodes that fell within the 300 x 300 μm^2 area on the surface of the plate. Taking the mean average of the values, one pixel for the IR camera was represented analytically. The numerical modeling data was gathered in the same manner (Fig. 4-c), and the method of interpreting the data provided a reasonable comparison among all case studies.

Resulting individual line scans are observed for each of the line passes for each case study; analytical method, numerical method, and experimental results. Shown in Figure 5-a, data from the experimental case study is shown in its entirety. Due to the large amount of data collected for each case study, single line scans represented as maximum peak temperatures were explored for information on cooling rates (Fig. 5-b). Exampled with the 225 W laser power parameter, maximum distance between two consecutive peaks is equidistance (Fig. 5-b), indicating the data that was collected through the analytical and numerical methods was accurately meshed with cell size appropriate to capture maximum temperature peaks. This also confirms that the experimental data was able to provide reasonable resolution of the experiment to compare with the models. Due to the limitation of the IR camera minimum temperature reading of 600 °C, cooling rate detail below this threshold is not captured in the experimental results.

4.2. Thermal Histories and Cooling Trends

The thermal history results of the analytical method, numerical method, and experimental runs are overlaid and shown in Figure 6, and summarized in Table 2. The analytical method shows a steep symmetrical increase and decrease in CR, with continuous exponential growth in the maximum temperature. There are reasonable explanations for the behavior seen in the analytical method. Exponential growth in modeling such as the analytical model in this research has been seen in previous research, where laser absorptivity phenomenon occurs when the surface temperature is not explicitly capped at the boiling point, causing heat flux to increase exponentially [30, 10, 31]. The absorptivity phenomenon was possibly due to the heat transfer assumptions of the model, specifically with how conduction is represented through temperature-dependent material properties (heat capacity and thermal conductivity) given in Equation 8. This type of error was seen in the numerical method prior to adjusting conduction boundary conditions to allow for nonconforming meshing. As mentioned in the methods section, the meshing was built to optimize mesh size by creating higher resolution at the surface. Non-conforming mesh allowed for the solver to more accurately capture heating and cooling curves for each scan. As a result of more accurate boundary conditions, the numerical method trended more closely to the experimental results and was able to better align both heating and cooling rates with those of the experimental than what the analytical method could predict.

The change in maximum temperature that occurs from 75 W (Fig. 6-a) to 150 W (Fig. 6-b) increases in all cases, while the change from 150 W (Fig. 6-b) to 225 W (Fig. 6-c) decreases in both the numerical method and experimental runs only. Additionally, both the numerical and experimental results show a steep heating rate with a lower CR, consistent with expected results from previous studies on INC625 laser processing [32, 33, 34]. The numerical method shows good agreement with the experimental results. The maximum temperature had an average error of 9%, while the CR had an average error of 4%. These differences align with literature reported average errors ranging from 9-24% [21, 31] for simulation modeling.

Table 2. The maximum temperatures and cooling rates for analytical and numerical simulations and experimental results of Inconel 625 plate scan for 75 W, 150 W, and 225 W.

Method	Trial	Max Temp. (°C)	CR ($^{\circ}C \cdot s^{-1}$) Single Line Scan
Analytical	75 W	951	$1.3\text{x}10^4$
	150 W	1877	$4.1\text{x}10^4$
	225 W	2470	$5.4\text{x}10^4$
Numerical	75 W	950	$2.0\text{x}10^4$
	150 W	1771	$2.7\text{x}10^4$
	225 W	1623	$2.2\text{x}10^4$
Experimental	75 W	1304	$1.6\text{x}10^4$
	150 W	1719	$2.8\text{x}10^4$
	225 W	1720	$2.4\text{x}10^4$

A stable or decreasing maximum temperature and CR from 150 W to 225 W is observed (Table 2) in the numerical method and experimental results, possibly due to INC625 material properties such as thermal conductivity, heat capacity, and surface tension which could allow for a thermal increase shown as a deeper penetration rather than surface temperature result. This can be explained through works examining melt pool dimensions where the increase in laser power increases melt pool dimensions both horizontally and vertically [21]. According to the heat conduction equation, thermal conduction and convective heat transfer contribute to heat flow, so with the high conductivity of INC625 it is possible that the heat at the higher laser power of 225 W was not reflected as a higher maximum temperature in the surface examined because of the larger area that was being impacted by the heat transfer process.

4.3. Cooling Trends and Microstructural Evolution

Unprocessed and processed samples for each of the laser powers were analyzed using Inverse Pole Figure (IPF) mapping through EBSD imaging in order to understand the impact of heat on the build plate from a depth standpoint. Results are shown in

Figure 7 in both the parallel and perpendicular scan directions as described in Figure 3, where the parallel scan direction corresponds to the x and z axes and the perpendicular scan direction corresponds to the y and z axes. Analysis of the laser effected area is shown with thick black borders within each sample to emphasize the area of interest within each base plate.

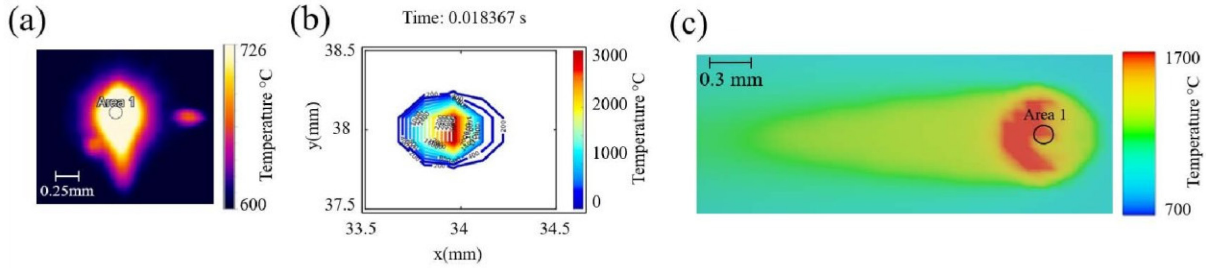

Figure 4. Temperature gradient for (a) IR camera experiment data output, (b) analytical model using double-elliptical heat source, and (c) numerical.

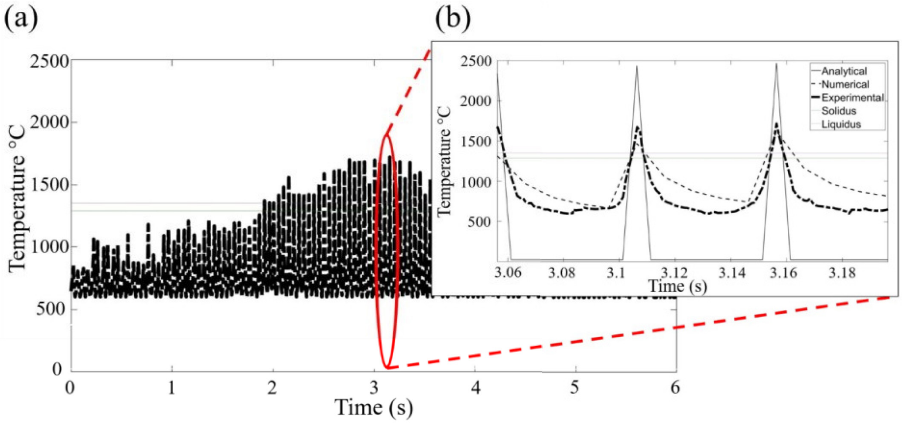

Figure 5. Segregated line scan results for (a) 225 W experimental results and (b) snapshot of individual line scans for analytical model, numerical model, and experimental results.

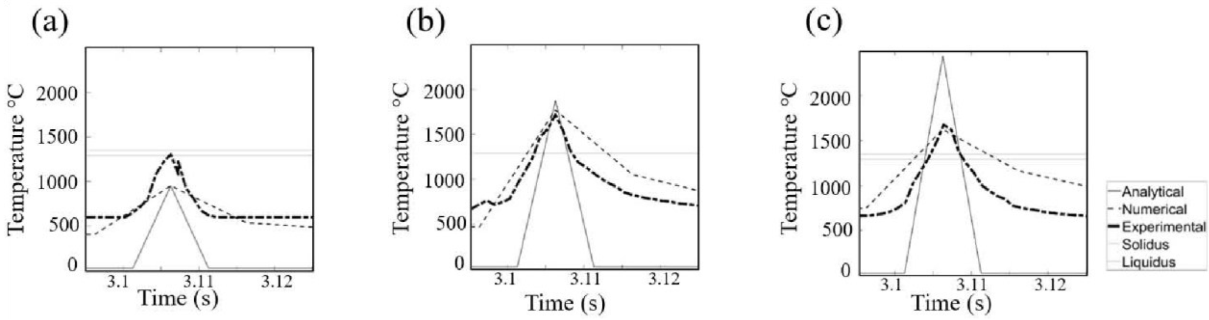

Figure 6. Maximum temperature line scan (single line scans at center point of the plate) results for analytical, numerical, and experimental thermal profiles of (a) 75 W, (b) 150 W, (c) 225 W.

The unprocessed samples shown in Figures 7-a-b exhibit a random grain orientation, typically seen in unprocessed INC625. The first direction shows a slightly higher orientation towards a < 001 > direction, which is commonly found in unprocessed INC625. EBSD imaging in the parallel scan direction for 75 W exhibits generally columnar elongated grains, with equiaxed grains at the surface (Fig. 7-c). This has been experienced previously in literature [35, 36].

Directionality of this 75 W sample in the parallel scan direction is non-dominant. In the perpendicular scan direction for 75 W (Fig. 7-d) the elongated grains extend from the surface and appear slightly curved. This phenomenon can be explained through a closer look at the spatial imaging of the laser scan, where the strength of heat flow is prioritized first through thickness and second laterally, where the lateral heat flow is generated perpendicular relative to the scan [37, 38]. The difference between parallel and perpendicular grain orientation is reported in prior work [37, 39, 40, 41], explaining why the perpendicular scan direction exhibits long columnar grains extending to the surface, while the parallel scan direction results in equiaxed at the surface with columnar grains beneath as each pass of the laser advances at 20 µm hatch spacing with each line scan. Another possible explanation for this phenomenon could be through its relationship to the high orthotropic properties of INC625, where these elastic properties in two or three planes could be perpendicular to each other. Elastic properties of INC625 as they relate to processing

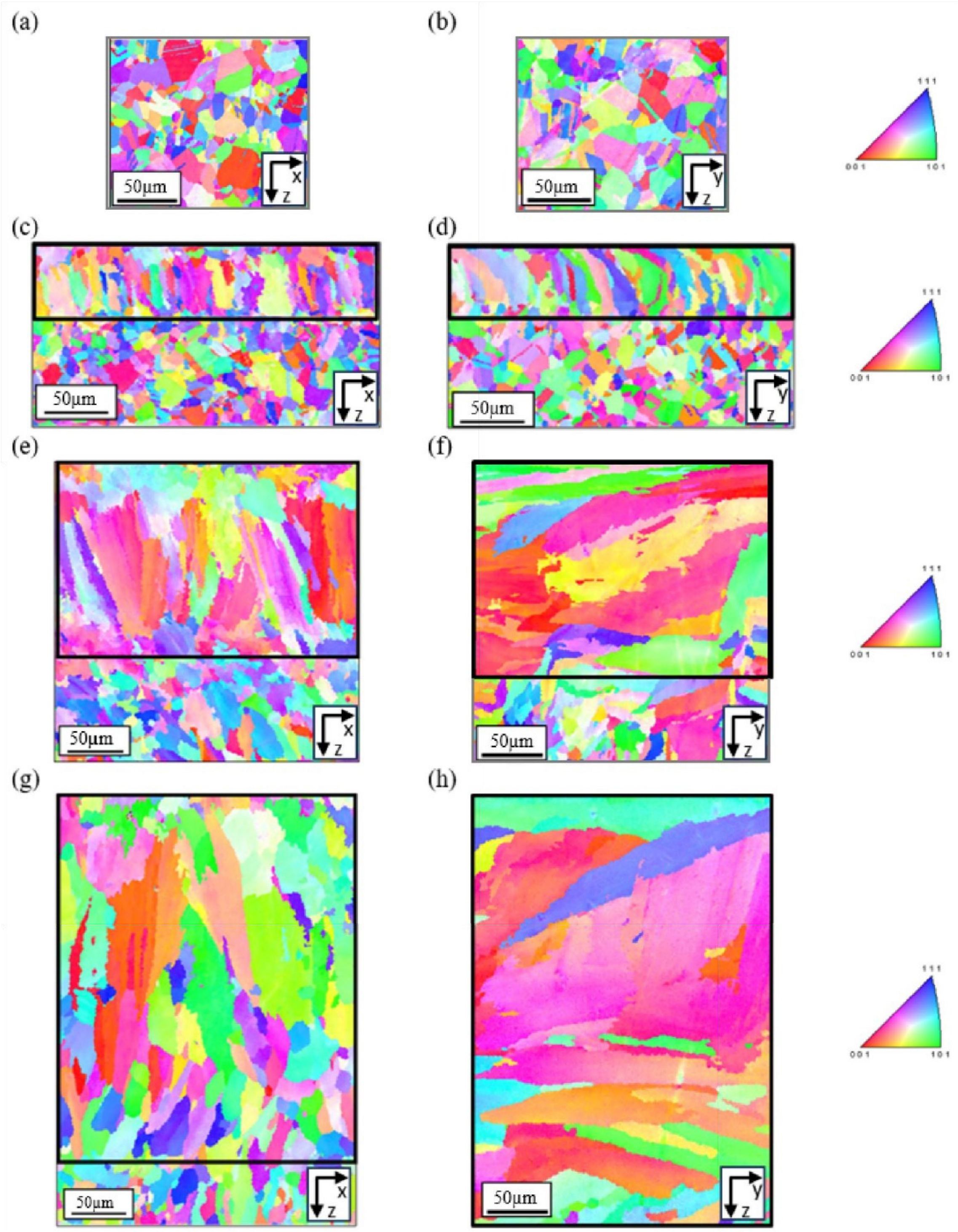

Figure 7. EBSD imaging of laser plate scan for: unprocessed sample in (a) first direction and (b) second direction; 75 W in (c) parallel and (d) perpendicular scan direction; 150 W in (e) parallel and (f) perpendicular scan direction; 225 W in (g) parallel and (h) perpendicular scan direction. **Dark boxes indicate area for scan analysis of grain size.

parameters have been discussed in literature [38], but have not been deeply explored.

The IPF maps for 150 W are shown in Figures 7-e-f and it can

the grains increases from the 75 W samples, and a stronger movement from vertical columnar grains to horizontal columnar grains is observed, likely due to the stronger direction of heat flow as mentioned above. It is shown by Zhou et al. [42] that in Ni-based materials with FCC structure, (100) planes align with the fastest heat transfer direction. The majority of red be seen again that the parallel scan direction exhibits equiaxed within the IPF maps (Figs. 7-e-f) show the < 001 > direction is grains on the top surface with columnar grains beneath, while normal to the 150 W sample.

the perpendicular scan direction shows columnar grains. In

both scan directions for the 150 W laser power the thickness of

150 W to 225 W (Fig. 7-e-h), the size of the grains deepens in the z-direction as the depth of heat increases and results in longer and wider grains. The evolution in grain size from 75 W to 150 W to 225 W is related to the laser power where as melt pool size increases the grain size also increases. As shown in Figure 8, increasing laser power results in increasing grain size in terms of diameter as a function of area fraction. However, in the parallel scan direction (Fig. 8-a), it is shown that the 150 W laser parameter resulted in larger diameter grains than 225 W. Based on the understanding that at a single point in time the CR dropped from 150 W to 225W (Table 2), this result aligns with our heat flow discussion and is validated in the perpendicular scan direction shown in Figure 8-b as a significant increase from 150 W to 225 W in grain size diameter. This indicates the heat flow in the perpendicular scan direction dominated over the parallel scan direction.

The evolution of microstructure observed in the experimental results is explained through the trending maximum surface temperature and CR (caused by laser power and scan speed, respectively) that are observed in both the numerical method and experimental results. While the drop in maximum surface temperature and CR at 225 W was not an expected outcome, the consistency with numerical modeling and experimental results validates the use of laser power manipulation as one means of tailoring the microstructure. This observation is evidence of the importance in understanding the thermal history within laser processing and the value that using a numerical method for modeling can provide to understanding laser processing parameter impact on final properties. As demonstrated in previous work, solidification microstructure can be examined and customized by understanding heat flow effect on grain evolution through the use of coupling numerical modeling methods (such as the one presented in this research) with methods such as cellular automation method [43], an area of simulation investigation worth further exploration to better understand and predict the process-microstructure relationship.

4.4. Comparison of Analytical and Numerical Models

In contrast, the analytical method ran using 1 core at a time per simulation on an Intel Xeon Gold 6130 CPU 2.10 GHz running on a high-performance cluster. By using a cluster, all simulations could be ran simultaneously and took roughly 55 minutes to complete. Additionally, the analytical model parameters used the suggested shape coefficients from Goldak et al. [12] for the heat source model, which means that the

While the general orientation of grains for both parallel and

perpendicular scan directions does not change drastically from model may be less accurate with alloys that do not fit this general assumption well. In terms of simulation time, the analytical method proved advantageous for running parametric studies, particularly those used to determine trending patters where multiple simulation runs are necessary. However, changes to model assumptions would need to occur to account for significant melt pool behavior changes and material properties for materials such as Inconel 625 in order to provide more meaningful results.

Although the solving methods used in the numerical model are optimized for simplicity, the predictions are computationally expensive. Ran locally on 10 cores on an Intel i9-10900 2.80 GHz processor, the numerical method took advantage of these cores for solving and completed each simulation in 6.0 hours. The accuracy of the numerical method to experiment was far superior to the analytical method, better accounting for conductivity through the build plate and providing thermal history that could be related to microstructural evolution. The numerical method proved to be a better solution for exploring complex alloys such as Inconel 625.

5. Conclusions

This study presents analytical and numerical methods that predict time-dependent thermal history based on process parameters during laser processing of INC625. Both methods were compared against experimental results with respect to accuracy and efficiency. Experimental samples were analyzed in terms of microstructural evolution with respect to laser power increase and related to thermal history. The key findings of the study include:

(1) The analytical method resulted in a significantly steep CR and exponential maximum temperature with increased laser power as compared to that of both the numerical method and experimental results. This was likely caused by the representation of conduction in the models heat transfer assumptions along with the complex material properties of INC625. This made the analytical method not well suited in this work.

(2) The numerical method predicted thermal history and CR in good agreement with experimental results, with heat transfer accurate in providing a link to predicting tailored microstructure through thermal control.

(3) While the analytical method is less computationally expensive, it was not a good fit for modeling laser processing of INC625. Contrastingly, the numerical method proved superior for accurate thermal predictions for heat flow analysis that could be related to tailoring of microstructure.

6. Acknowledgements

This work relates to Department of Navy award (Award Number N00014-20-1-2836 in collaboration with University of Tennessee, Knoxville) issued by the Office of Naval Research. The United States Government has a royalty-free license throughout the world in all copyrightable material contained herein. Any opinions, findings, and conclusions or recommendations expressed in this material are those of the author(s) and do not necessarily reflect the views of the Office of Naval Research. The authors acknowledge and thank Stefan Ball for his initial work on developing the analytical and numerical models, and experimental design. Authors also thank Dongqing Yan for their experimental support and valuable feedback.

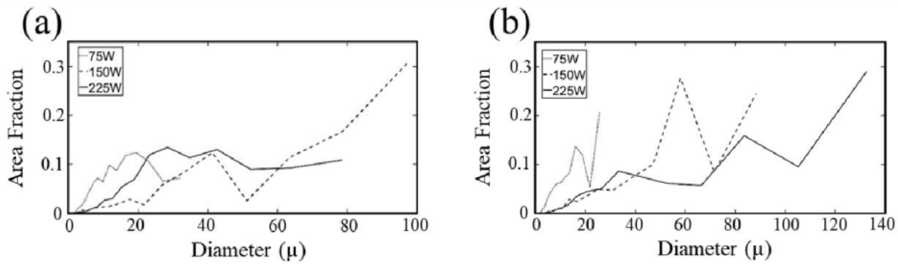

Figure 8. Comparison of the grain size diameter for sampled laser powers of 75 W, 150 W, and 225 W in scan directions (a) parallel and (b) perpendicular.

References

[1] Y. Huang, M. Ansari, H. Asgari, M. H. Farshidianfar, D. Sarker, M. B. Khamesee, E. Toyserkani, Rapid prediction of real-time thermal characteristics, solidification parameters and microstructure in laser directed energy deposition (powder-fed additive manufacturing), Journal of Materials Processing Technology 274 (2019) 116286. doi:10.1016/j.jmatprotec.2019.116286.
URL https://linkinghub.elsevier.com/retrieve/pii/ S0924013619302584

[2] C. Pleass, S. Jothi, Influence of powder characteristics and additive manufacturing process parameters on the microstructure and mechanical behaviour of Inconel 625 fabricated by Selective Laser Melting, Additive Manufacturing 24 (2018) 419–431. doi:10.1016/j.addma.2018.09.023.
URL https://linkinghub.elsevier.com/retrieve/pii/ S2214860418303518

[3] S. David, J. Vitek, R. Reed, T. Hebble, Effect of rapid solidification on stainless steel weld metal microstructures and its implications on the Schaeffler diagram, Tech. Rep. ORNL/TM-10487, 5957599 (Sep. 1987). doi: 10.2172/5957599.
URL http://www.osti.gov/servlets/purl/5957599-qV53lw/

[4] S. Ghorbanpour, K. Deshmukh, S. Sahu, T. Riemslag, E. Reinton, E. Borisov, A. Popovich, V. Bertolo, Q. Jiang, M. T. Sanchez, M. Knezevic, V. Popovich, Additive manufacturing of functionally graded inconel 718: Effect of heat treatment and building orientation on microstructure and fatigue behaviour, Journal of Materials Processing Technology 306 (2022) 117573. doi:10.1016/j.jmatprotec.2022.117573.
URL https://linkinghub.elsevier.com/retrieve/pii/ S0924013622000851

[5] Z. Yu, Y. Zheng, J. Chen, C. Wu, J. Xu, H. Lu, C. Yu, Effect of laser remelting processing on microstructure and mechanical properties of 17-4 PH stainless steel during laser direct metal deposition, Journal of Materials Processing Technology 284 (2020) 116738. doi:10.1016/j.jmatprotec.2020.116738.
URL https://linkinghub.elsevier.com/retrieve/pii/ S0924013620301527

[6] A. Clare, R. Mishra, M. Merklein, H. Tan, I. Todd, L. Chechik, J. Li, M. Bambach, Alloy design and adaptation for additive manufacture, Journal of Materials Processing Technology 299 (2022) 117358. doi:10.1016/j.jmatprotec.2021.117358.
URL https://linkinghub.elsevier.com/retrieve/pii/ S0924013621003186

[7] T. Mukherjee, H. Wei, A. De, T. DebRoy, Heat and fluid flow in additive manufacturing – Part II: Powder bed fusion of stainless steel, and titanium, nickel and aluminum base alloys, Computational Materials Science 150 (2018) 369–380. doi:10.1016/j.commatsci.2018.04.027.
URL https://linkinghub.elsevier.com/retrieve/pii/ S0927025618302684

[8] H. Rezaeifar, M. A. Elbestawi, On-line melt pool temperature control in LPBF additive manufacturing, The International Journal of Advanced Manufacturing Technology 112 (9-10) (2021) 2789–2804. doi:10.1007/ s00170-020-06441-0.
URL http://link.springer.com/10.1007/s00170-020-06441-0

[9] N. Kouraytem, X. Li, W. Tan, B. Kappes, A. D. Spear, Modeling process–structure–property relationships in metal additive manufacturing: a review on physics-driven versus data-driven approaches, Journal of Physics: Materials 4 (3) (2021) 032002. doi:10.1088/2515-7639/abca7b.
URL https://iopscience.iop.org/article/10.1088/ 2515-7639/abca7b

[10] P. Promoppatum, S.-C. Yao, P. C. Pistorius, A. D. Rollett, A Comprehensive Comparison of the Analytical and Numerical Prediction of the Thermal History and Solidification Microstructure of Inconel 718 Products Made by Laser Powder-Bed Fusion, Engineering 3 (5) (2017) 685–694. doi:10.1016/J.ENG.2017.05.023.
URL https://linkinghub.elsevier.com/retrieve/pii/ S2095809917307208

[11] D. Rosenthal, Mathematical theory of heat distribution during welding and cutting, Welding 20 (5) (1941) 220–234.

[12] J. Goldak, M. Bibby, J. Moore, R. House, B. Patel, Computer modeling of heat flow in welds, Metallurgical Transactions B 17 (3) (1986) 587–600. doi:10.1007/BF02670226.
URL https://doi.org/10.1007/BF02670226

[13] S. V. Chernyshikhin, D. G. Firsov, I. V. Shishkovsky, Selective Laser Melting of Pre-Alloyed NiTi Powder: Single-Track Study and FE Modeling with Heat Source Calibration, Materials 14 (23) (2021) 7486. doi: 10.3390/ma14237486.
URL https://www.mdpi.com/1996-1944/14/23/7486

[14] Y. Yang, X. Zhou, Q. Li, C. Ayas, A computationally efficient thermomechanical model for wire arc additive manufacturing, Additive Manufacturing 46 (2021) 102090. doi:10.1016/j.addma.2021.102090.
URL https://linkinghub.elsevier.com/retrieve/pii/ S2214860421002554

[15] N. Nguyen, J. H. Chujutalli, Simulating convective-radiative heat sink effect by means of FEA-based Gaussian heat sources and its approximate analytical solutions for semi-infinite body, The International Journal of Advanced Manufacturing Technology 117 (11-12) (2021) 3717–3742. doi:10.1007/s00170-021-07699-8.
URL https://link.springer.com/10.1007/ s00170-021-07699-8

[16] D. Gery, H. Long, P. Maropoulos, Effects of welding speed, energy input and heat source distribution on temperature variations in butt joint welding, Journal of Materials Processing Technology 167 (2-3) (2005) 393–401. doi:10.1016/j.jmatprotec.2005.06.018.
URL https://linkinghub.elsevier.com/retrieve/pii/ S0924013605005819

[17] S. Bag, A. Trivedi, A. De, Development of a finite element based heat transfer model for conduction mode laser spot welding process using an adaptive volumetric heat source, International Journal of Thermal Sciences 48 (10) (2009) 1923–1931. doi:10.1016/j.ijthermalsci.2009.02.010.
URL https://linkinghub.elsevier.com/retrieve/pii/ S1290072909000349

[18] E. Mirkoohi, D. E. Seivers, H. Garmestani, S. Y. Liang, Heat Source Modeling in Selective Laser Melting, Materials 12 (13) (2019) 2052, number: 13 Publisher: Multidisciplinary Digital Publishing Institute. doi: 10.3390/ma12132052.
URL https://www.mdpi.com/1996-1944/12/13/2052

[19] W. Jamrozik, J. Górka, B. Wygle̢dacz, M. Kiel-Jamrozik, FEM-Based Thermogram Correction for Inconel 625 Joint Hardness Clustering, Materials 15 (3) (2022) 1113. doi:10.3390/ma15031113.
URL https://www.mdpi.com/1996-1944/15/3/1113

[20] D. Youssef, S. Hassab-Elnaby, S. R. Al-Sayed, New 3D model for accurate prediction of thermal and microstructure evolution of laser powder cladding of Ti6Al4V alloy, Alexandria Engineering Journal (2021) S1110016821006189doi:10.1016/j.aej.2021.09.014.
URL https://linkinghub.elsevier.com/retrieve/pii/ S1110016821006189

[21] J. K. Chaurasia, A. Jinoop, P. P, C. Paul, K. Bindra, S. Bontha, Study of melt pool geometry and solidification microstructure during laser surface melting of Inconel 625 alloy, Optik 246 (2021) 167766. doi:10.1016/j.ijleo.2021.167766.
URL https://linkinghub.elsevier.com/retrieve/pii/ S0030402621013590

[22] Z. Luo, Y. Zhao, Efficient thermal finite element modeling of selective laser melting of Inconel 718, Computational Mechanics 65 (3) (2020) 763–787. doi:10.1007/s00466-019-01794-0.
URL http://link.springer.com/10.1007/s00466-019-01794-0

[23] Y. Gu, Y. D. Li, Y. Yong, F. L. Xu, L. F. Su, Determination of parameters of double-ellipsoidal heat source model based on optimization method, Welding in the World 63 (2) (2019) 365–376. doi:10.1007/ s40194-01800678-w.
URL https://doi.org/10.1007/s40194-018-00678-w [24] FLOW3D® (2019).

[25] C. Hirt, B. Nichols, Volume of fluid (VOF) method for the dynamics of free boundaries, Journal of Computational Physics 39 (1) (1981) 201–225. doi:10.1016/0021-9991(81)90145-5.
URL https://linkinghub.elsevier.com/retrieve/pii/ 0021999181901455

[26] K. Ren, Y. Chew, J. Fuh, Y. Zhang, G. Bi, Thermo-mechanical analyses for optimized path planning in laser aided additive manufacturing processes, Materials & Design 162 (2019) 80–93. doi:10.1016/j.matdes.2018.11.014.
URL https://linkinghub.elsevier.com/retrieve/pii/ S0264127518308207

[27] J. Coleman, A. Plotkowski, B. Stump, N. Raghavan, A. S. Sabau, M. J. M. Krane, R. E. Ricker, L. Levine, S. S. Babu, Sensitivity of Thermal Predictions to Uncertain Surface Tension Data in Laser Additive Manufacturing, Journal of Heat Transfer (2019) 27.

[28] W. Ursine, F. Calado, G. Teixeira, H. Diniz, S. Silvino, R. De Andrade, Thermal / Visible Autonomous Stereo Visio System Calibration Methodology for Non-controlled Environments, in: Proceedings of the 2012 International Conference on Quantitative InfraRed Thermography, QIRT Council, 2012. doi:10.21611/qirt.2012.261.
URL http://qirt.org/archives/qirt2012doi/papers/ QIRT-2012-261.pdf

[29] T. G. Spears, S. A. Gold, In-process sensing in selective laser melting (SLM) additive manufacturing, Integrating Materials and Manufacturing Innovation 5 (1) (2016) 16–40. doi:10.1186/s40192-016-0045-4.
URL http://link.springer.com/10.1186/s40192-016-0045-4

[30] C. A. Fletcher, Computational techniques for fluid dynamics 2: Specific techniques for different flow categories., Springer Science & Business Media, 2012.

[31] Z. Gan, Y. Lian, S. E. Lin, K. K. Jones, W. K. Liu, G. J. Wagner, Benchmark Study of Thermal Behavior, Surface Topography, and Dendritic Microstructure in Selective Laser Melting of Inconel 625, Integrating Materials and Manufacturing Innovation 8 (2) (2019) 178–193. doi:10.1007/ s40192-01900130-x.
URL http://link.springer.com/10.1007/s40192-019-00130-x

[32] P. Nie, O. Ojo, Z. Li, Numerical modeling of microstructure evolution during laser additive manufacturing of a nickel-based superalloy, Acta Materialia 77 (2014) 85–95. doi:10.1016/j.actamat.2014.05.039.
URL https://linkinghub.elsevier.com/retrieve/pii/ S1359645414003875

[33] M. N. Dogu, K. Davut, M. A. Obeidi, M. A. Yalçın, H. Gu, T. S. E.˘ Low, J. Ginn, D. Brabazon, Recrystallization and grain growth kinetics of IN718 manufactured by laser powder bed fusion, Journal of Materials Research and Technology 19 (2022) 4242–4257. doi:10.1016/j.jmrt.2022.06.157.
URL https://linkinghub.elsevier.com/retrieve/pii/ S2238785422010183

[34] X. Fang, H. Li, M. Wang, C. Li, Y. Guo, Characterization of texture and grain boundary character distributions of selective laser melted Inconel 625 alloy, Materials Characterization 143 (2018) 182–190. doi:10.1016/j.matchar.2018.02.008.
URL https://linkinghub.elsevier.com/retrieve/pii/ S1044580317331583

[35] G. Knapp, N. Raghavan, A. Plotkowski, T. DebRoy, Experiments and simulations on solidification microstructure for Inconel 718 in powder bed fusion electron beam additive manufacturing, Additive Manufacturing 25 (2019) 511–521. doi:10.1016/j.addma.2018.12.001.
URL https://linkinghub.elsevier.com/retrieve/pii/ S2214860418306973

[36] Y. P. Lei, H. Murakawa, Y. W. Shi, X. Y. Li, Numerical analysis of the competitive in¯uence of Marangoni ¯ow and evaporation on heat surface temperature and molten pool shape in laser surface remelting, Computational Materials Science (2001) 15.

[37] S. Li, Q. Wei, Y. Shi, Z. Zhu, D. Zhang, Microstructure Characteristics of Inconel 625 Superalloy Manufactured by Selective Laser Melting, Journal of Materials Science & Technology 31 (9) (2015) 946–952. doi:10.1016/j.jmst.2014.09.020.
URL https://linkinghub.elsevier.com/retrieve/pii/ S1005030215000663

[38] A. Khabouchi, P. Ventura, N. Leymarie, A. Hazotte, L. Germain, Crystallographic texture and velocities of ultrasonic waves in a Ni-based superalloy manufactured by laser powder bed fusion, Materials Characterization 169 (2020) 110607. doi:10.1016/j.matchar.2020.110607.
URL https://linkinghub.elsevier.com/retrieve/pii/ S1044580320320787

[39] D. Ma, A. D. Stoica, Z. Wang, A. M. Beese, Crystallographic texture in an additively manufactured nickel-base superalloy, Materials Science and Engineering: A 684 (2017) 47–53. doi:10.1016/j.msea.2016.12.028.
URL https://linkinghub.elsevier.com/retrieve/pii/ S0921509316315180

[40] A. Tabei, E. Mirkoohi, H. Garmestani, S. Liang, Modeling of texture development in additive manufacturing of Ni-based superalloys, The International Journal of Advanced Manufacturing Technology 103 (1-4) (2019) 1057–1066. doi:10.1007/s00170-019-03555-y.
URL http://link.springer.com/10.1007/s00170-019-03555-y

[41] G. Dinda, A. Dasgupta, J. Mazumder, Texture control during laser deposition of nickel-based superalloy, Scripta Materialia 67 (5) (2012) 503– 506. doi:10.1016/j.scriptamat.2012.06.014.
URL https://linkinghub.elsevier.com/retrieve/pii/ S1359646212003983

[42] Y. Zhou, A. Volek, N. Green, Mechanism of competitive grain growth in directional solidification of a nickel-base superalloy, Acta Materialia 56 (11) (2008) 2631–2637. doi:10.1016/j.actamat.2008.02.022.
URL https://linkinghub.elsevier.com/retrieve/pii/ S1359645408001055

[43] F. Xiong, Z. Gan, J. Chen, Y. Lian, Evaluate the effect of melt pool convection on grain structure of IN625 in laser melting process using experimentally validated process-structure modeling, Journal of Materials Processing Technology 303 (2022) 117538. doi:10.1016/j.jmatprotec.2022.117538. URL https://linkinghub.elsevier.com/retrieve/pii/S0924013622000504